3D printable magnesium-based cements towards the preparation of bioceramics

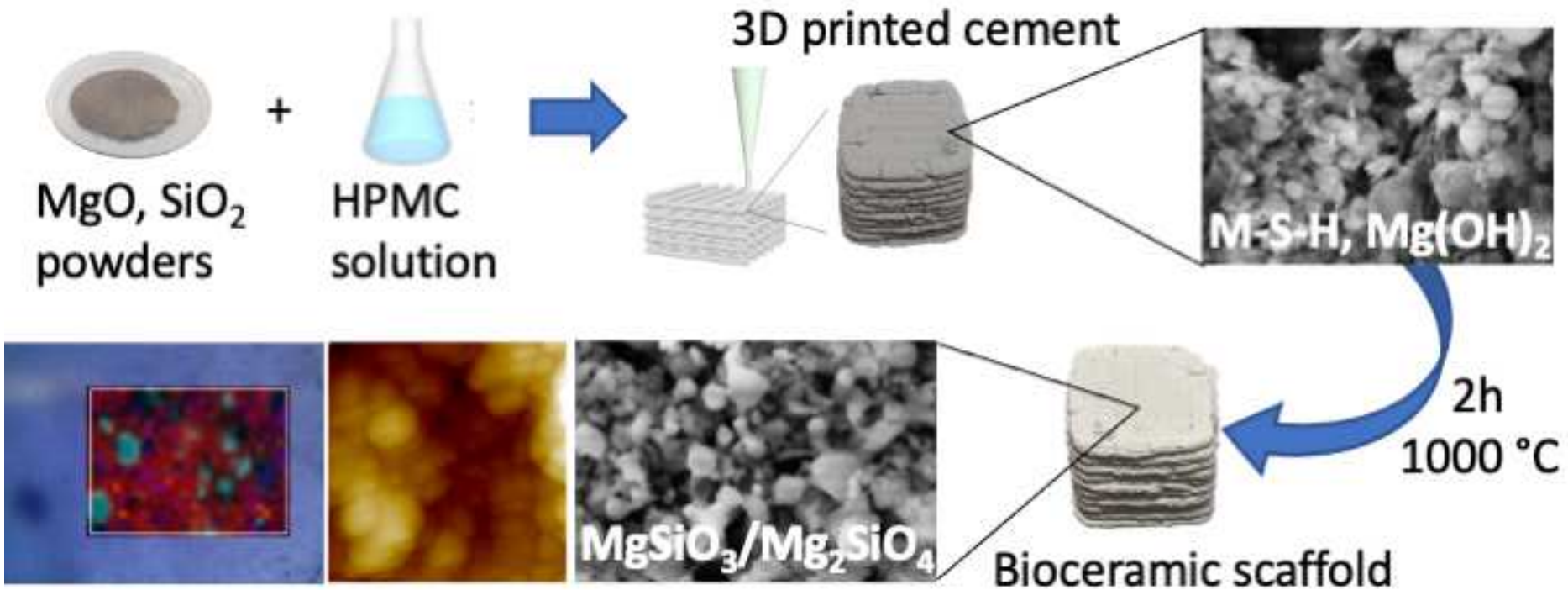

3D printable magnesium-based cements towards the preparation of bioceramics

Monica Tonelli, Andrea Faralli, Francesca Ridi, Massimo Bonini*

Department of Chemistry "Ugo Schiff" and CSGI, University of Florence, via della Lastruccia 3, 50019 Sesto Fiorentino, Florence, Italy. E-mail: monica.tonelli@unifi.it; andrea.faralli@stud.unifi.it; francesca.ridi@unifi.it; massimo.bonini@unifi.it

* corresponding author: Massimo Bonini

E-mail: massimo.bonini@unifi.it

Tel: +39 055 4573014

Address: Department of Chemistry "Ugo Schiff" and CSGI, University of Florence, via della Lastruccia 3, Sesto Fiorentino, 50019 Florence, Italy.

Abstract

Hypothesis: Among all the materials used so far to replace and repair damaged bone tissues, magnesium silicate bioceramics are one of the most promising, thanks to their biocompatibility, osteoinductive properties and good mechanical stability.

Experiments: Magnesium silicate cement pastes were prepared by hydration of MgO mixed with different SiO_2 batches at different Mg/Si molar ratios. Pastes were either moulded or 3D printed to obtain set cements that were then calcined at 1000 °C to produce biologically relevant ceramic materials. Both cements and ceramics were characterized by means of X-ray diffraction, while two selected formulations were thoroughly characterized by means of injectability tests, Raman confocal microscopy, scanning electron microscopy, atomic force microscopy, gas porosimetry, X ray microtomography and compressive tests.

Findings: The results show that bioceramic scaffolds, namely forsterite and clinoenstatite, can be effectively obtained by 3D printing MgO/SiO_2 cement pastes, paving the way towards important advances in the field of bone tissue engineering.

Keywords

MgO/SiO_2 cements; Magnesium silicate hydrate; Forsterite; Clinoenstatite; bone tissues engineering; Cancellous bone replacement composite; 3D printed porous scaffold.

Abbreviations

M-S-H: magnesium silicate hydrate; HPMC: hydroxypropyl methylcellulose; PDF: Powder Diffraction Files; SM: Supplementary Material; SSA: Specific Surface Area; PSD: Pore Size Distribution; BET: Brunauer-Emmet-Teller method; BJH: Barrett-Joyner-Halenda analysis; AFM: Atomic Force Microscopy.

1. Introduction

Silicate bioceramics recently attracted considerable attention in the field of tissue regeneration and have been used for the replacement and repair of damaged hard tissues since the beginning of the century.[1–3] Many methods have been used to prepare bioactive ceramics as porous scaffolds for bone tissue engineering, including foam templating, freeze-casting, directional crystallization and porogen techniques,[4,5] but conventional approaches have shown several limitations: the scaffold geometry and its pores' morphology, size, and interconnections, which should be fine-tuned for the specific case of application, are hard to control.[6] 3D printing, as one of the extrusion technology-based rapid prototyping techniques, introduces numerous advantages, allowing for the precise control of the porous structure of a broad spectrum of different materials.[7,8] In the past two decades, many porous bioceramic scaffolds for bone tissue reconstruction have been 3D printed, including calcium phosphates,[5] hydroxyapatite ceramics,[9] calcium silicates[10] and bioactive glasses.[11] In conventional approaches, calcium phosphate and silicate ceramics and glasses are fabricated using either organic binders, which are burned out after printing by means of high temperature calcination, or reactive calcium-based cements, exploiting their hydraulic setting reaction.[4,12]

In recent years many synthetic materials have been considered for bone-regenerative applications[13] and magnesium-based bioceramics emerged as a new class of promising biodegradable materials, due to their good degradation and biocompatibility.[14,15] In particular, clinoenstatite ($MgSiO_3$) and forsterite (Mg_2SiO_4) recently received increasing attention, thanks to their good cytocompatibility, osteo-stimulatory activity, mechanical stability and good degradation rate.[15–24] Clinoenstatite and forsterite can be synthesized via precipitation method, to obtain gels that need to be heated at very high temperature for obtaining the crystalline bioceramics. $MgSiO_3$ powders are typically prepared using magnesium nitrate and sodium silicate,[23] while Mg_2SiO_4 can be prepared starting from magnesium carbonate and talc powder,[25] from magnesium nitrate and $Si(OC_2H_5)_4$,[19] from magnesium nitrate and colloidal silica[26] or through transient liquid phase effect with fused magnesia and quartz.[27] In other cases, forsterite was also prepared by solid state reaction, using precursors of MgO and SiO_2 mixed by ball-milling,[28] or preparing a slurry of the powders in a large excess of water.[29] In case of sol-gel or precipitation processes, the product of the synthesis, before the heating, is an amorphous gel phase, referred to as magnesium silicate hydrate (M-S-H). M-S-H is already well known in the literature in other applications, not connected to bioceramic materials. As a matter of fact, M-S-H is the

binder gel phase of one of the most interesting eco-sustainable alternative cements,[30–34] widely used for the encapsulation of radioactive wastes.[35–38] Magnesium-based cements are generally obtained by mixing MgO or $Mg(OH)_2$ with silica, and the reaction proceeds through the hydration of periclase (MgO) to give brucite ($Mg(OH)_2$), which then reacts with SiO_2 to produce M–S–H gel.[31,32,34] Some of the authors recently reported a full characterisation of M-S-H, which was found to be constituted by a mixture of sub-nanometric domains with local structure resembling those of chrysotile ($Mg_3Si_2O_5(OH)_4$) and talc ($Mg_3Si_4O_{10}(OH)_2$).[39] When calcined at high temperatures, chrysotile converts to a mixture of forsterite and clinoenstatite,[40] while talc converts to clinoenstatite.[39,41,42] Thus, it seems possible to prepare clinoenstatite and/or forsterite bioceramic materials also by heating M-S-H binder phase prepared starting from MgO/SiO_2 cements.

In this study, magnesium silicate cement pastes were prepared by hydration of MgO mixed with different SiO_2 batches at two different Mg/Si molar ratios. Pastes were either moulded or 3D printed to obtain set cements, that were then calcined at 1000 °C to produce ceramic materials, and the phase composition of both cements and ceramics was assessed by means of X ray diffraction (XRD). In the literature, the use of MgO/SiO_2 binders in 3D printing was reported only once, very recently, and the authors demonstrated that this cement paste can be extruded to design building components.[43] In our work, for the first time MgO/SiO_2 cements were printed and calcined to obtain 3D printed scaffold bioceramics, that were thoroughly characterized by means of Raman confocal microscopy, scanning electron microscopy (SEM), atomic force microscopy (AFM), gas porosimetry, X ray microtomography and compressive tests.

2. Experimental

2.1 Materials

Periclase (MgO, ≥ 99 % trace metals basis, 325 mesh) was supplied by Sigma-Aldrich. The reactivity of periclase was measured according to the test proposed by van der Merwe et al.[44] and resulted to be 80 s, indicating that the powder is highly reactive. Magnesium based cements were prepared using different silica sources: Silica Fumed was purchased from Aldrich (SiO_2 99.8%, particle size 0.007 μm, BET specific surface area = 399 m^2/g), SYLOID® 244 FP Silica was kindly provided by Grace (SiO_2 > 95 %, BET specific surface area = 527 m^2/g), Silica Gel 60 was purchased from Fluka (Analytical SiO_2, 230-400 mesh, BET specific surface area = 410 m^2/g), Elkem Microsilica® Grade 940 U was kindly provided by Elkem (dry silica fume,

SiO_2 > 90 %, BET specific surface area = 4.33 m^2/g). Hydroxypropyl methylcellulose (HPMC) was purchased from Sigma-Aldrich. Milli-Q water was used throughout all the experiments. All materials were used as received, without any further purification.

2.2 Samples' Preparation

The samples prepared and characterized throughout this study are sketched in Figure 1. First, cement pastes with different compositions were prepared. These cement pastes were either casted into moulds or 3D printed. They were then let set to obtain moulded cements and printed cements, respectively. The materials were then calcined at 1000 ˚C to convert them into moulded and printed bioceramics. The details of each step are given in the following sections.

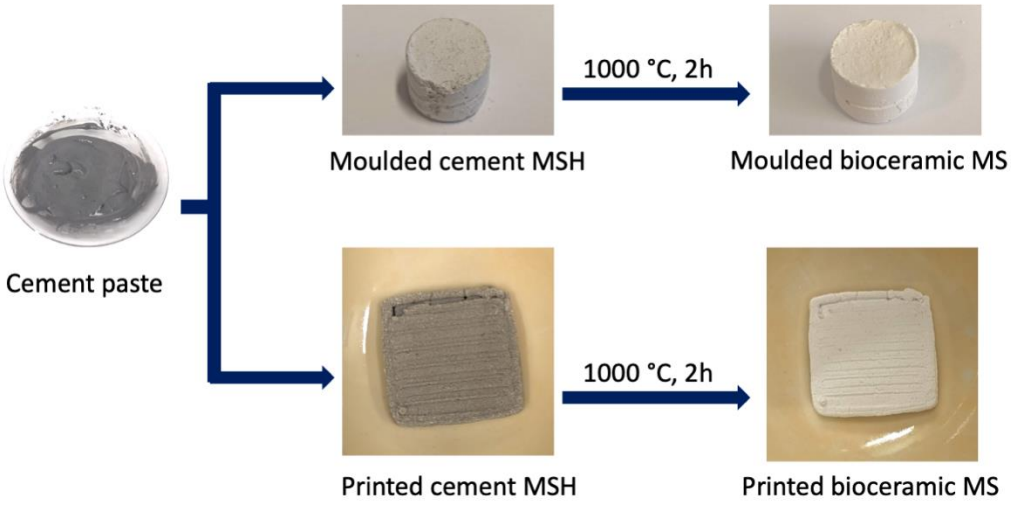

Figure 1. Schematic diagram of samples' preparation and characterization pathways.

2.2.1 Preparation of magnesium-based cement pastes

Cements were typically prepared by mixing MgO and SiO_2 in a 1/1 or 2/1 molar ratio. The two powders were accurately dry-mixed and then cement pastes were prepared by adding milliQ water. For the preparation of the moulded cement samples, pure water was used, while for the 3D printing of cements, a solution of HPMC in water (10 %wt) was used. The liquid-to-solid weight ratio (l/s) was adjusted case by case, using the minimal ratio needed to obtain a workable paste. The composition of the investigated pastes is reported in Table 1 together with the abbreviated notation used to refer to the samples throughout the paper. The MSH abbreviation was used to indicate that pastes consist of magnesium silicate hydrates.

Table 1. Composition of the investigated cement samples.

abbreviated notation	type of silica	Mg/Si molar ratio	liquid/solid ratio (w/w)
MSH_fumed_1	fumed (Aldrich)	1	4
MSH_fumed_2	fumed (Aldrich)	2	4
MSH_syloid_1	syloid (Grace)	1	3
MSH_ syloid _2	syloid (Grace)	2	3
MSH_ gel _1	gel (Fluka)	1	1.2
MSH_ gel _2	gel (Fluka)	2	1.2
MSH_elkem_1	fume microsilica (Elkem)	1	1.25
MSH_ elkem _2	fume microsilica (Elkem)	2	1.25

In a typical experiment, after mixing for about 30 seconds, the cement pastes were either poured in plastic moulds of 1 cm-diameter (moulded cements) or 3D printed (printed cements). Moulded cements were set at room temperature and relative humidity > 96 % before characterization. Printed cements were stored at 25 °C or 37 °C and relative humidity > 96 % before characterization. Then, at predetermined times, roughly 1 g of set cement was withdrawn and freeze-dried to stop the hydration reaction.

2.2.2 Preparation of 3D printed cements

Scaffolds were printed using an Engine Standard Resolution 3D printer developed by HyRel, equipped with a modular head KRA-15, using a tapered G16 needle, at a modular dosing pressure. In this study, two macroporous structures were designed using FreeCAD program, sliced through slic3r program (Repetrel) and printed. The two shapes (20 x 20 x 3 mm^3 and 10 x 10 x 10 mm^3) were printed at 8 mm/s, with a layer thickness of 1 mm, at an infill ratio of 80 %. The file codes used to print the scaffolds are reported in the Supplementary Material (SM), together with the pictures of printed cements and printed bioceramics in the 3D shapes used throughout this work (Figure S1).

2.2.3 Preparation of magnesium silicate bioceramics

The bioceramics were prepared through the calcination of hardened cements. To this purpose, moulded and printed cements were heated in a muffle (Nabertherm) at 1000 °C for 2 h, to obtain crystalline ceramic materials. The samples resulting from the calcination of the different MSH samples reported in Table 1 are coded as MS (e.g., MS_fumed_1 is the sample obtained by heating MSH_fumed_1) to indicate that the hydrated phases were converted into dry phases.

2.3 Characterization Techniques

2.3.1 X-Ray Diffraction (XRD)

XRD data were collected with a D8 Advance with DAVINCI design (Bruker, Milan, Italy), using as X-rays source the Cu Kα radiation (wavelength λ= 1.542 Å), at 40 kV and 40 mA, a 2θ range of 5 – 70 °, a step size of 0.05 ° and a time/step of 0.3 s. Before the analysis, cements/bioceramics were grinded with mortar and pestle and flattened on the sample holder. Peaks' assignment was based on the Powder Diffraction Files (PDF) of the database of the International Centre for Diffraction Data.

2.3.2 Injectability tests

The injectability of the formulations was investigated by means of a built in house apparatus, applying specific loads to the same syringe and needle (tapered 16G) used for the 3D printing. By measuring the amount of extruded cement paste and knowing the density of the two tested cement pastes ($\delta_{MSH\_gel\_1}$ = 1358 kg/m^3, $\delta_{MSH\_elkem\_2}$ = 1470 kg/m^3), the volumetric flow rates were obtained as a function of the applied forces, allowing for the calculation of the apparent viscosity according to the Hagen-Poiseuille equation for tapered needles.[45]

2.3.3 Confocal Raman Microscopy

Raman analysis and mapping were performed with a Renishaw inVia Qontor confocal MicroRaman system equipped with a 532 nm laser (Nd:YAG solid state type, 50 mW, 1800 l/mm grating), front illuminated CCD camera and research-grade Leica DM 2700 microscope equipped with a 20x objective (theoretical spot size 2.4 μm). Raman spectra were acquired in the spectral range 170 - 1910 cm^{-1}, and maps were collected with a step size of 2.5 μm.

2.3.4 Field Emission-Scanning Electron Microscopy (FE-SEM)

FE-SEM images were collected on cements and bioceramics surfaces and cross-sections with a field-emission ΣIGMA microscope (Carl Zeiss Microscopy, Germany). Specimens were fixed on aluminum stubs by means

of conductive tape. The accelerating potential was 10.00 kV, while the working distance was ~ 8 mm. Images were acquired using InLens (10Kx – 250Kx) and standard (90x – 5Kx) secondary electrons detector.

2.3.5 Atomic Force Microscopy (AFM)

AFM was performed with a Park System XE-7 microscope equipped with PPP-CONTSCR probes (tip radius of curvature < 10 nm) in contact mode. Image processing (flattening) and calculation of the roughness parameters were performed using the Park Systems XEI software 1.8.2.

2.3.6 Gas porosimetry

The Specific Surface Area (SSA) and Pore Size Distribution (PSD) of the 3D printed bioceramics were measured by means of a Coulter SA 3100 analyser (Beckman Coulter), using nitrogen as adsorptive gas. The samples were broken into small pieces and inserted in the sample holders. Prior to the measurements, samples were outgassed for 30 min at 120 °C. SSA was obtained using the Brunauer-Emmet-Teller (BET) method,[46] while the pore size distribution was estimated using Barrett-Joyner-Halenda (BJH) analysis.[47]

2.3.7 X-ray Micro Computed Tomography

X-ray microtomography was performed with a SKYSCAN 1172 high-resolution XμCT scanner (Bruker) on the selected printed bioceramics. Experiments were performed at 100 kV and 100 μA, at a step size of 0.3 °, with a theoretical resolution of ~ 9 μm. Calculation of the porosity and image processing were performed using the NRecon Reconstruction Program software 1.7.4.6.

2.3.8 Compressive strength tests

The compressive strength of bioceramic scaffolds was tested by performing compression experiments using a custom-built apparatus. Cubic 3D printed specimens were subjected to a gradually increasing load, applied on the top surface until a rupture was observed. Five samples were prepared for each selected composition, and the reported results are the average ± the associated standard deviation.

3. Results and Discussion

Samples were investigated by multiple physico-chemical techniques aiming at understanding the effect of different silica sources and Mg/Si molar ratios on the formation of M-S-H in magnesium-based cements and on the formation of crystalline bioceramic materials after calcination. As described in detail in section 2.2.1, all cement pastes were prepared by mixing MgO and SiO_2 powders. For the preparation of mouldable cement

pastes, powders were mixed with pure water, while printable cement pastes were obtained using aqueous HPMC solutions. Moulded cements were characterized by means of XRD, to evaluate the formation of M-S-H binder phase. Afterwards, cements were calcined to obtain bioceramics, which were characterized again by means of XRD to check the formation of crystalline phases with potential biological applications, namely forsterite and enstatite. On the other hand, cement pastes containing HPMC were 3D printed and, once set, cement's phase composition was assessed by means of XRD, to confirm the presence of M-S-H and to investigate possible effects due to the presence of HPMC. Then, printed cements were calcined to obtain printed bioceramics that were characterized by Raman confocal microscopy, SEM, AFM, gas porosimetry, X-ray microtomography and compressive tests.

The results obtained from the characterizations of moulded cements, printed cements, and bioceramics are analysed and comprehensively discussed in the following sections.

3.1 Characterization of moulded cements

Magnesium-based moulded cements were investigated by XRD to check their phase composition and the results are reported in Figure 2. MSH_fumed_1 displays the characteristic peaks of amorphous M-S-H,[31,48] while both the diffraction peaks of M-S-H and crystalline $Mg(OH)_2$ in the form of brucite can be recognized in MSH_fumed_2.[38,49] Analogously, in MSH_syloid_1 only amorphous M-S-H binder phase is present, while both M-S-H and brucite are present in MSH_syloid_2. In MSH_gel_1 and MSH_gel_2, both M-S-H and brucite peaks can be recognized, brucite being more abundant in MSH_gel_2. MSH_elkem_1 and MSH_elkem_2 show similar diffractograms, with brucite clearly representing the main phase: in fact, the broad signals of M-S-H are almost entirely covered by the diffraction pattern of brucite. Summarizing, brucite is more abundant in all the formulations when Mg/Si = 2, indicating that increasing the amount of the available Mg^{2+} does not necessarily produce a higher amount of M-S-H, and that some phases remain unreacted also when using highly reactive silica, such as fumed SiO_2. On the other hand, when using gel or Elkem silica, brucite is the main phase irrespectively of the Mg/Si ratio, consistently with a lower reactivity of the powders.

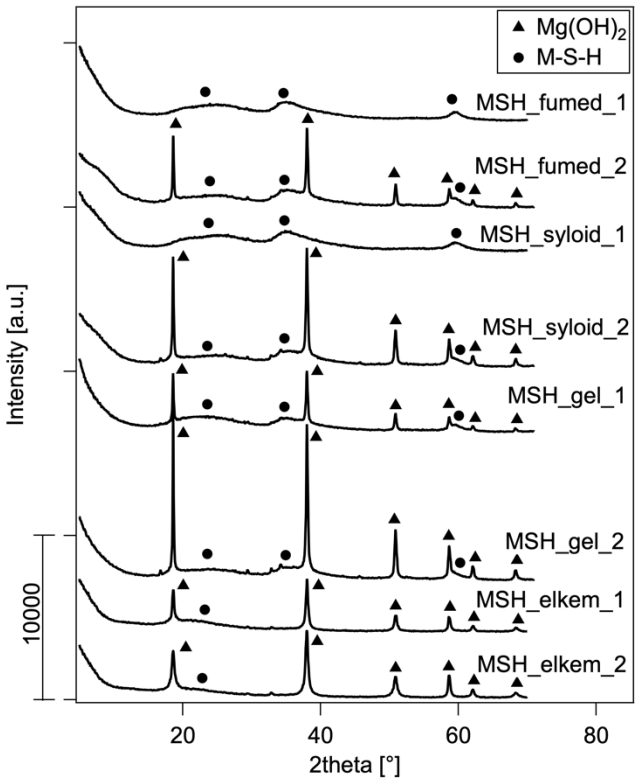

Figure 2. XRD patterns of cements after 7 days of hydration at 25 °C.

3.2 Characterization of magnesium silicate bioceramics

The results of the XRD experiments performed on the cements calcined after 7 days of hydration are reported in Figure 3. The pattern of MS_fumed_1 reveals the presence of clinoenstatite (AMCSD:0010589, COD: 9005775), while forsterite (AMCSD: 0000276, COD: 9013540) is present in MS_fumed_2, together with traces of MgO (AMCSD: 0000501, COD: 1000053) and clinoenstatite. MS_syloid shows a similar behaviour: MS_syloid_1 presents only the characteristic diffraction peaks of clinoenstatite, while MS_syloid_2 presents the characteristic peaks of forsterite, together with minor signals arising from MgO and clinoenstatite. MS_gel_1 and MS_gel_2 show similar patterns, described by a mixture of clinoenstatite and forsterite crystalline phases. Finally, MS_elkem_1 and MS_elkem_2 samples contain forsterite, together with MgO and cristobalite (AMCSD: 0001629, COD: 9008110), a mineral polymorph of silica that forms at very high temperatures. In MS_elkem_2 MgO is more abundant than in MS_elkem_1, as evident from the comparison of the peaks assigned to forsterite and MgO. Thus, the formation of bioceramics is influenced both by the silica source and Mg/Si ratio. When M-S-H is the main phase in the cement, this binding gel entirely converts into clinoenstatite/forsterite during calcination. When brucite is the main phase, calcination produces again

clinoenstatite/forsterite, together with MgO and SiO_2 arising from unreacted $Mg(OH)_2$ and silica. Remarkably, also where M-S-H is present in small amount, the calcination still leads to the formation of crystalline bioceramic materials.

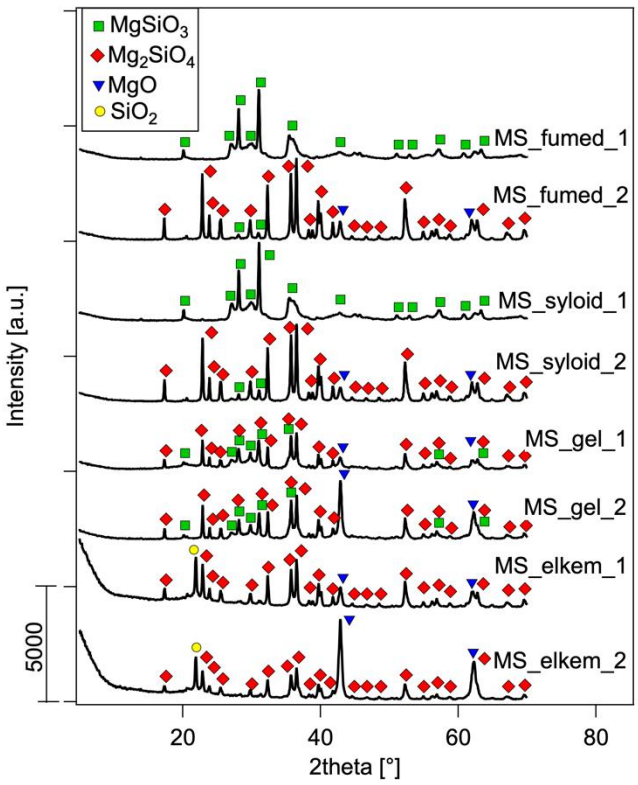

Figure 3. XRD patterns of bioceramics prepared through the thermal treatment of set cements after 7 days of hydration at 25 °C. Clinoenstatite ($MgSiO_3$), Forsterite (Mg_2SiO_4), Magnesia (MgO) and Cristobalite (SiO_2) are indicated by the corresponding markers.

In the cases of gel and Elkem silicas, as no sample with a predominant phase was obtained after 7 days of setting, we evaluated the effect of longer hydration times. XRD diffractograms of MS_gel and MS_elkem samples calcined after 28 days of hydration are reported in Figure S2 in the Supplementary Material. According to the results, MS_gel_1 and MS_gel_2 show different patterns if calcined after 28 days of hydration: MS_gel_1 shows the characteristic peaks of clinoenstatite, while MS_gel_2 shows the characteristic peaks of forsterite. On the other hand, MS_elkem_1 and MS_elkem_2 samples calcined after 7 or 28 days of hydration show similar patterns, described by the presence of forsterite, MgO, SiO_2 and traces of clinoenstatite. MgO is more abundant in the samples calcined after 7 days, but it is still present in the samples calcined after

28 days, while unreacted SiO_2 is no more present after 28 days. This trend is consistent with previous literature reports,[39] highlighting that longer curing periods (28 days instead of 7 days) allows M-S-H phase to rearrange while the hydration reaction proceeds, which in turns affects the ceramic phases that form upon heating.

3.3 3D printing and characterization of printed cements

Printable MgO/SiO_2 formulations were obtained by mixing the powders with a 10 %wt HPMC water solution: in fact, pastes prepared with pure water show poor flowability and, when used in 3D printing, it was impossible to obtain a steady flow during the injection. Replacing water with a 10 %wt HPMC aqueous solution, it was possible to obtain a good printability for all the investigated samples. As a matter of fact, HPMC is an ideal binder in bioceramics, being a biocompatible, biodegradable, hydrophilic polymer.[50–52] It is also important to remark here, that it could be possible to use specific additives to adjust the rheological properties of cement pastes and influence their printability, as recently reported by Panda et al.[43], that prepared 3D printing building components using MgO/SiO_2 using sodium hexametaphosphate as plasticizer.[53] Pictures of printed cements are shown in Figure 4 (on the left), together with the images of the same samples after calcination (on the right). The structural resistance shows a clear difference on the type of silica used in the cement paste. In particular, cements containing fumed silica and Syloid did not withstand the calcination, irrespectively of the Mg/Si ratio. In the case of MSH_gel, the formulation prepared using Mg/Si = 1 showed a slightly better structural resistance to calcination than the one prepared using Mg/Si = 2. On the contrary, with Elkem silica the formulation prepared using Mg/Si = 2 was more resistant than the one prepared at Mg/Si = 1. As shown in Fig. 4, two formulations were found to successfully preserve their shape after calcination: MSH_gel_1 and MSH_elkem_2. Pictures of the 3D printouts obtained with selected formulations are reported in Figure S1 in the SM. In the case of Elkem, the size of the object after its printing and subsequent calcination differs from the original 3D design by less than 1 mm, with a reasonably good accuracy for most of the applications envisionable for clinoenstatite/forsterite-based materials in bone tissue engineering. When using Silica Gel, the control is less accurate: in fact, in this case, the accuracy between the original 3D design and the final material is within 2 mm, suggesting a preference for Elkem-based formulations when the 3D printing is required.

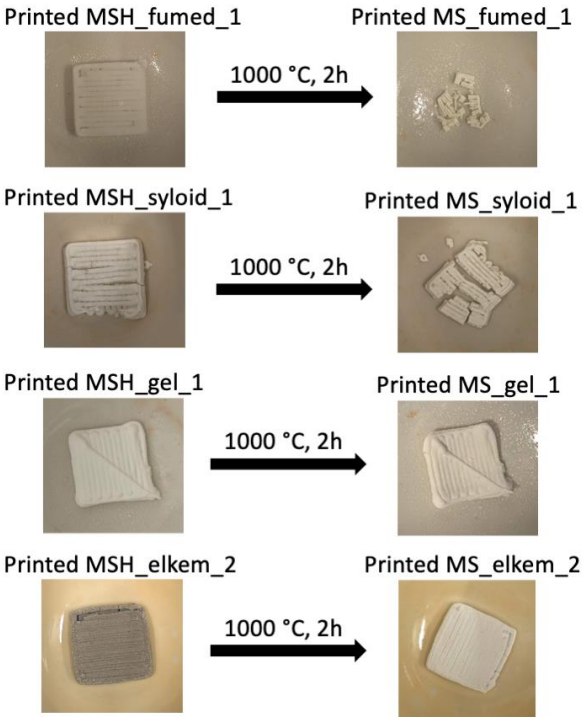

Figure 4. Pictures of printed cements and printed bioceramics.

It is worth noting that, concerning their appearance, some of the cements display a greyish colour (especially MSH_elkem), due to the presence of carbonaceous residues present in traces. After calcination, all the bioceramics display a bright white colour, highlighting that all the residues are entirely decomposed.

Aiming at understanding the potential effect of the presence of HPMC on the phase compositions of ceramics, XRD results on moulded and printed bioceramics were compared. According to the results (see Figure S3 in the SM), the presence of HMPC does not affect the composition in terms of forming crystalline phases.

The injectability properties of the two selected formulations were investigated with a built in house apparatus (see Figure 5A). Different loads were applied to achieve a constant and homogeneous extrusion from the syringe (a video is available as supplementary material) and the measured volumetric flow rates were used to extract the apparent viscosity. The apparent viscosity η^*in a complex system can be defined as:

$$\eta^* = \tau_w/\dot{\gamma}^n \quad (1)$$

where τ_w is the wall shear stress and $\dot{\gamma}^n$ is the shear rate (with n=1 for Newtonian fluids). Applying the Hagen-Poiseulle law for tapered needles, the apparent viscosity is defined as:[45]

$$\eta^* = \frac{3F_{eff}D_{in}^3D_{out}^3 tan\theta}{16Q_tD_p^2(D_{in}^3 - D_{out}^3)} \quad (2)$$

where Q_t is the volumetric flow and the relevant geometrical parameters of syringe and needle D_p, D_{in}, D_{out} and $tan\theta$ are defined as in Figure 5A. F_{eff} is the effective injection force and it is calculated by subtracting the frictional force (calculated by measuring the minimal load necessary to achieve a stable extrusion of an HPMC water solution 10 wt%) to the force applied during cement paste extrusion. Figures 5B and 5C show the measured volumetric flow rate and the calculated apparent viscosity as a function of the injection force for MSH_gel_1 and MSH_elkem_2 samples, respectively. In both cases, it was found that a stable flow is obtained when the injection force approaches 30 N, followed by a shear-thinning behaviour when the force is further increased. Nevertheless, the two formulations present significantly different rheological behaviours in the investigated range: in fact, a nearly linear trend of the apparent viscosity *versus* the injection force was found for MSH_elkem_2, while an abrupt decrease was found for MSH_gel_1. Furthermore, a slightly higher force is required to obtain a stable flow in the case of MSH_gel_1 and, most importantly, its apparent viscosity is significantly larger than MSH_elkem_2. This behaviour is consistent with the poorer shape control in MSH_gel_1 3D printouts.

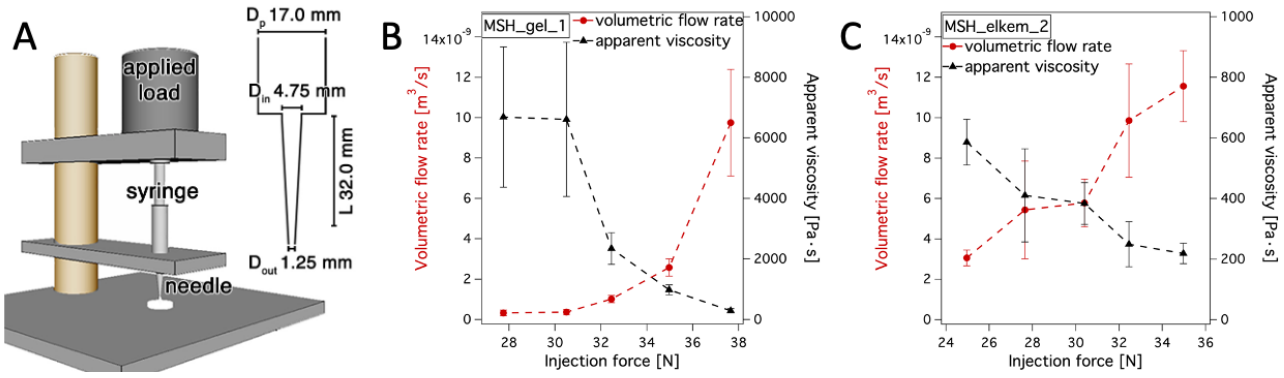

Figure 5. A) scheme of the apparatus used for the injectability test; B) volumetric flow rate and apparent viscosity as a function of the injection force of MSH_gel_1; C) volumetric flow rate and apparent viscosity as a function of the injection force of MSH_elkem_2.

We also evaluated the possibility to shorten the preparation protocol by increasing the curing temperature of the cements from 25 ºC to 37 ºC.[54] Since we observed that moulded and printed samples display the same phases, we evaluated the effect of the curing temperature on the composition only on the 3D printed selected ceramics. To this purpose, printed MSH_gel_1 and MSH_elkem_2 were stored at 37 °C, instead of 25 °C,

before calcination. By comparing the printed bioceramics prepared by heating the printed cements set at 37 °C or 25 °C we gained information on the effect of the temperature, and we evaluated the possibility of accelerating the preparation of the scaffolds. According to the results (XRD diffractograms reported in Figure S4 in the SM), no relevant differences were found by comparing samples cured for one week at 25 °C and cured for 2 days at 37 °C. MS_gel_1 prepared by heating MSH_gel_1 cured 2 days at 37 °C contains a mixture of clinoenstatite and forsterite, while MS_elkem_2 prepared by heating MSH_elkem_2 cured 2 days at 37 °C contains mainly forsterite. Prolonged times of curing at 37 °C before the calcination of cements do not affect the composition of the ceramic samples, suggesting that curing the samples for 2 days at 37 °C is ideal for accelerating the synthesis protocol.

3.4 Characterization of printed bioceramics

The selected printed bioceramics (MS_gel_1 and MS_elekem_2) were analysed in triplicate in order to investigate the formed phases, the morphology and the microstructure, especially focusing on the surface, which is relevant towards a potential application as a scaffold for bone tissue engineering. The replicates were used to evaluate the variability in the systems and to confirm the consistency of the samples in terms of visual aspect, phase composition, roughness, porosity and compressive strength. Confocal Raman microscopy (see Figure 6) was used to map both the surfaces and the cross-sections. No significant differences were observed between the exposed surfaces and the internal cross-sections of the samples. Furthermore, we confirmed that printed bioceramics expose the same chemical composition of their moulded counterparts (reported in section 3.2). MS_gel_1 contains a mixture of forsterite (RRUFF ID: R050117) and clinoenstatite (RRUFF ID: X050038), while MS_elkem_2 mainly contains forsterite, with some impurities arising from the used silica (SiC (RRUFF ID: 110106), Si (RRUFF ID: R050145) cristobalite, SiO_2 (RRUFF ID: X050049)).

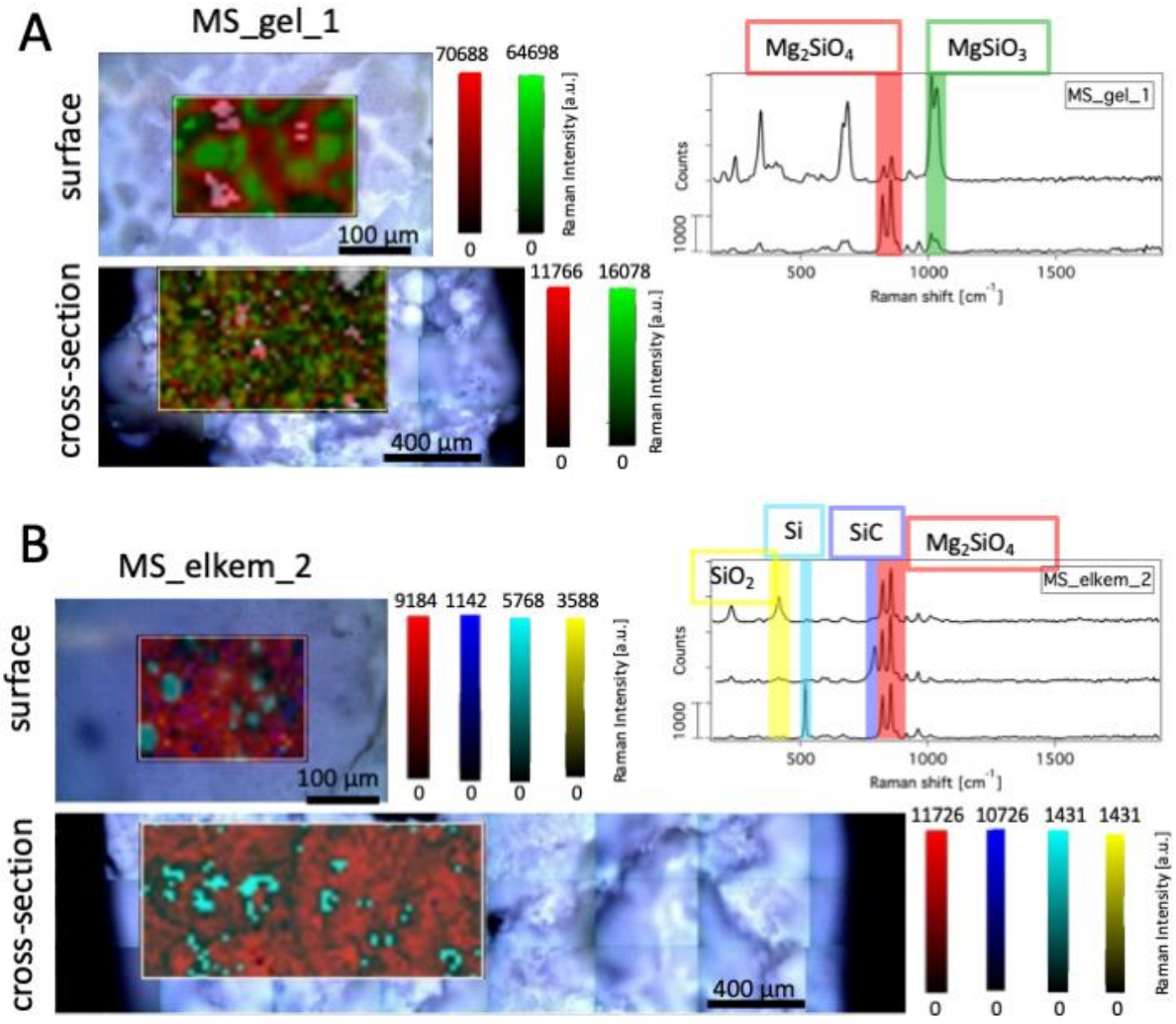

Figure 6. White light images and confocal Raman maps collected on the surfaces and cross-sections of printed MS_gel_1 (A) and MS_elkem_2 (B), together with some representative Raman spectra of the samples where the coloured regions highlight the peaks selected for the mapping. The white light images were obtained by means of a "montage" procedure, in order to display the entire cross-sections.

Figure 7 shows the SEM images collected on the surfaces and cross-sections of printed MS_gel_1 and MS_elkem_2. In both cases the morphology of the samples is quite homogeneous. At small magnifications we can see the porous morphology of the samples. The surface of MS_gel_1 shows the presence of cracks and we can identify the different printing layers (Fig. 7A, image on the top left). At higher magnifications (Fig. 7A, image in the centre), no separation between the printing layers can be found, suggesting an optimal bonding between them. In MS_elkem_2 (Fig. 7B) we cannot even distinguish the different printing layers. In the images collected at high magnification (images on the right) we can recognize in both samples agglomerated flakes-

like objects and particles, most reasonably attributed to $MgSiO_3$ or Mg_2SiO_4.[19,23,24] The presence of some unreacted MgO or SiO_2 cannot be excluded.

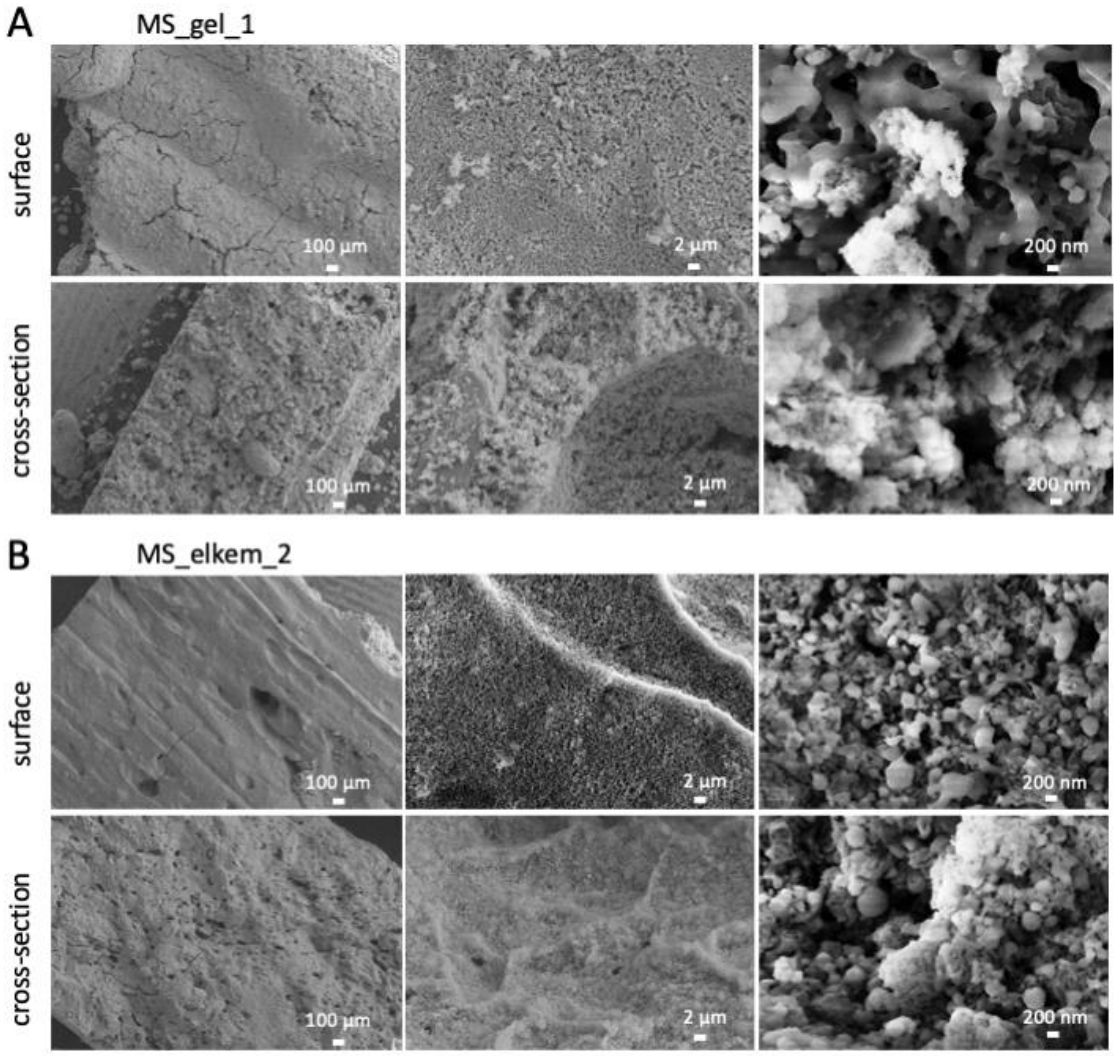

Figure 7. FE-SEM images of the surfaces and cross-sections of the printed bioceramics MS_gel_1 (A) and MS_elkem_2 (B).

The topography of the printed bioceramics was investigated by means of AFM, reported in Figure 8. The surfaces display a topography with rounded particles whose size approximately ranges from tens of nm to 2 microns. The samples, exposing a micro-structured rough surface, display similar values of roughness (R_a, arithmetic mean roughness): 144 ± 31 nm for MS_gel_1 and 117 ± 26 nm for MS_elkem_2. Similar values were recently reported for the successful deposition of hydroxyapatite on composite scaffolds made of wollanstonite/forsterite,[55,56] suggesting a good compatibility with biological applications.[57–59]

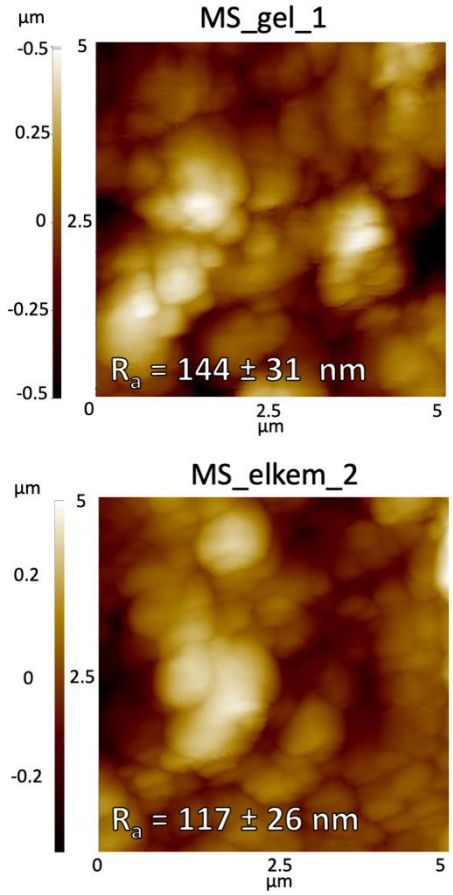

Figure 8. AFM maps of printed MS_gel_1 (top) and MS_elkem_2 (bottom). The reported arithmetic mean roughness values are the average of 3 maps acquired on different regions of the samples ± standard deviation.

Gas porosimetry, X-ray micro computed tomography and compressive test were used to gain information on the microstructure porosity and structural resistance: the results are reported in Table 2 and Figures 9 and 10. Specific surface area and total pore volume were obtained through gas porosimetry, that access nano-scale porosity, while the estimated porosity was obtained from micro-tomography and refers to micrometric pores. According to the results (see Figure 9 and Table 2), MS_gel_1 has a lower surface area and total pore volume than MS_elkem_2, indicating that in MS_gel_1 the nanoscale pores are less abundant. The two physisorption isotherms calculated from gas porosimetry for MS_gel_1 and MS_elkem_2 samples are compatible with the existence of aggregates that give rise to polydisperse porosity in the range from micropores to macropores (see Figure 9A).[60–62] The pore size distributions calculated by means of BJH method (see Figure 9B) display two main populations of pores for both samples (diameter of ~ 40 nm and ~ 100 nm), which could allow for the store of drug molecules.[63] The porosity accessed by BET/PSD experiments (3 – 200 nm) depends on the

structures' phases, and can be associated to the complex network of pores typical of dried cementitious materials.[64] In fact, the porous distribution of M-S-H binder phase is characterized by pores ranging from few to tens of nanometers, and it is influenced by the original voids between MgO and silica particles/agglomerates, into which water can enter promoting magnesium silicate precipitation. The porous structure at the nano-scale of the ceramics after the calcination is directly related to the structure of M-S-H in the cements.

Concerning the porosity at the microscale (see Figures 9C and 10), MS_gel_1 shows some cracks and a higher porosity value than MS_elkem_2. The pore size distribution calculated from X-ray micro computed tomography evidenced some differences between the two samples: MS_gel_1 presents 2 populations of micrometric pores (diameter of ~ 40 μm and ~ 100 μm), while MS_elkem_2 displays one main population of micrometric pores (~ 40 μm). These differences most reasonably rely on the diverse composition of these samples, but it is important to remark here that the porosity of the scaffolds at the micro- and macro-scale, when necessary, can be further controlled through the 3D printing, which allows for the design of porous structure.[7,8]

The compressive strengths measured with a custom-built apparatus resulted in a value of 0.32 ± 0.03 MPa for MS_gel_1 and 0.38 ± 0.03 MPa for MS_elkem_2, which are potentially appropriate for applications as scaffolds for cancellous bone,[65] and significantly higher than Mg-silicate scaffolds prepared by means of traditional foam replica and sol–gel techniques.[17]

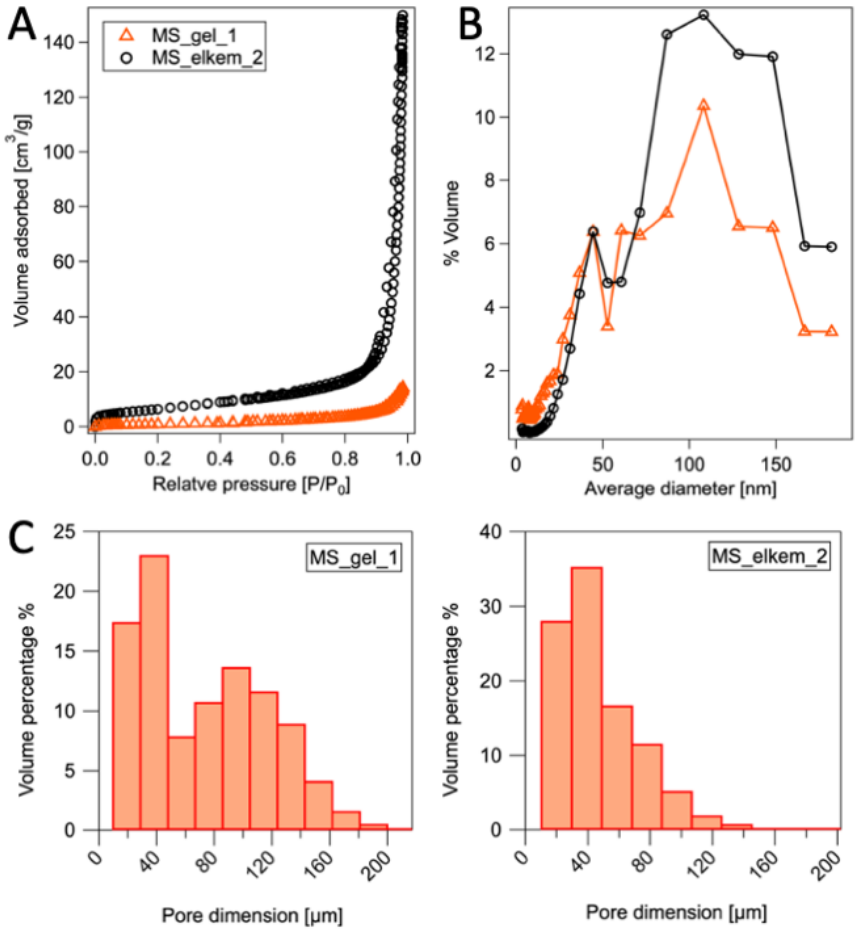

Figure 9. A) Nitrogen adsorption/desorption isotherms of printed MS_gel_1 and MS_elkem_2; B) Pore volume distribution calculated with BJH method from gas porosimetry experiments; C) Estimated pore size distribution of 3D printed MS_gel_1 (left) and MS_elkem_2 (right) samples calculated from X-ray micro computed tomography.

Table 2. SSA, total pore volume, estimated porosity and results of the preliminary compressive strength tests of the investigated printed bioceramics. SSA and total pore volume were obtained through gas porosimetry using the BET and BJH methods respectively, while the estimated porosity was calculated by means of X-ray micro computed tomography. The compressive strength values are the average of 5 tests ± standard deviation.

Sample	SSA (m^2/g)	Total Pore Volume (mL/g)	Estimated Porosity (%)	Compressive Strength (MPa)
MS_gel_1	3.44	0.020	20	0.32 ± 0.03
MS_elkem_2	23.4	0.196	8	0.38 ± 0.03

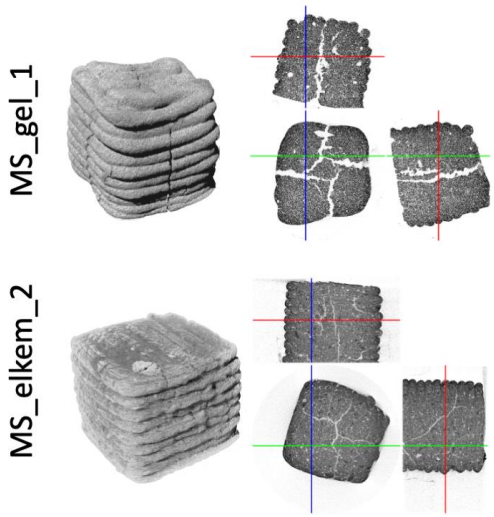

Figure 10. 3D computed X-ray micro tomography images and slice images of printed MS_gel_1 (top) and MS_elkem_2 (bottom).

4. Conclusions

The results presented in this paper show that crystalline bioceramics can be prepared through the calcination of either moulded or 3D printed magnesium silicate hydrate cements. The hydration of MgO/SiO_2 produces cement pastes made of both M-S-H binder and brucite, in different relative amounts depending on the silica source and the Mg/Si ratio. Noteworthy, increasing the magnesium amount results in a higher brucite content. Setting temperature and setting time are also relevant, as they affect the hydration reaction and the structural features of the M-S-H binding phase.[39] It is worth mentioning that the structural features on the molecular and sub-nanometric scale, as well as the proportions between chrysotile-like and talc-like domains, might influence the bioceramic phases forming during calcination.[39,40,42] In our samples, increasing the setting temperature from RT to 37 ºC takes to a consistent acceleration of the hydration reaction, consistently with what already reported in the literature for similar systems,[54] allowing for the shortening of the bioceramics preparation protocol. During the calcination, all samples convert to clinoenstatite and/or forsterite, two crystalline phases with potential interesting applications in the biomedical field.[15,18,19] Small amounts of MgO and SiO_2, arising from unreacted phases, are also detected in bioceramic samples where brucite was the main cement phase. No differences in the phase composition occur when HPMC is included in the formulations to obtain printable pastes. Only selected 3D printed cements samples structurally tolerate the calcination:

MS_gel_1 (silica gel and Mg/Si = 1) and MS_elkem_2 (elkem silica and Mg/Si = 2), and we also observed some differences in terms of shape retention when using different silica. Since the 3D printing process is driven by the injectability of the samples, the volumetric flow rate and the apparent viscosity of these samples were correlated to different injection forces. Then, taking into account potential applications of these bioceramics in the biomedical field, especially as bone regenerative scaffolds, we thoroughly characterized their surface properties, of outmost importance. Confocal Raman mapping shows that the surface of 3D printed bioceramics expose the same chemical composition of their moulded counterparts. SEM and AFM display good bonding between the different printing layers and homogeneously rough surfaces (100 nm < R_a < 150 nm), well-suited for the deposition of hydroxyapatite[55,56] and compatible with biological applications.[57–59] The pore size distributions obtained by BET/PSD experiments display two populations of pores for both samples (diameter of ~ 40 nm and ~ 100 nm), which could allow for the storage of drug molecules,[63] that reflects into the porous structure of the ceramics after the calcination. The calcination takes also to the formation of micrometric pores and cracks, as detected by X-ray micro-tomography. The selected 3D printed bioceramics, despite the presence of micrometric cracks, show compressive strength values (average value about 0.35 MPa) much higher than Mg-silicate scaffolds prepared by foam replica and sol–gel techniques (~ 0.005 MPa),[17] and potentially appropriate for applications as scaffolds for cancellous bone.[65] In future developments, the possibility to adjust the process parameters (such as the printing flux and the infill percentage) during the 3D printing[66,67] allows to target the proper balance between the size and the interconnectivity of the pores of the scaffold,[3] so to favour tissue ingrowth and vascularization, and appropriate mechanical properties.[65]

Acknowledgements

CSGI (Consorzio Interuniversitario per lo Sviluppo dei Sistemi a Grande Interfase), Fondazione CR Firenze (project 2017.0720) and MIUR-Italy ("Progetto Dipartimenti di Eccellenza 2018–2022" allocated to Department of Chemistry "Ugo Schiff") are acknowledged for financial support.

Dr. Samuele Ciattini and Dr. Laura Chelazzi (CRIST, University of Florence) are gratefully acknowledged for their technical support with the X-ray micro computed tomography experiments and analyses.

References

[1] W. Zhang, C. Feng, G. Yang, G. Li, X. Ding, S. Wang, Y. Dou, Z. Zhang, J. Chang, C. Wu, X. Jiang, 3D-printed scaffolds with synergistic effect of hollow-pipe structure and bioactive ions for vascularized bone regeneration, Biomaterials. 135 (2017) 85–95. https://doi.org/10.1016/j.biomaterials.2017.05.005.

[2] Y. Zhou, C. Wu, J. Chang, Bioceramics to regulate stem cells and their microenvironment for tissue regeneration, Mater. Today. 24 (2019) 41–56. https://doi.org/10.1016/j.mattod.2018.07.016.

[3] H. Zhu, D. Zhai, C. Lin, Y. Zhang, Z. Huan, J. Chang, C. Wu, 3D plotting of highly uniform $Sr_5(PO_4)_2SiO_4$ bioceramic scaffolds for bone tissue engineering, J. Mater. Chem. B. 4 (2016) 6200–6212. https://doi.org/10.1039/C6TB01692H.

[4] C. Yang, X. Wang, B. Ma, H. Zhu, Z. Huan, N. Ma, C. Wu, J. Chang, 3D-Printed Bioactive Ca_3SiO_5 Bone Cement Scaffolds with Nano Surface Structure for Bone Regeneration, ACS Appl. Mater. Interfaces. 9 (2017) 5757–5767. https://doi.org/10.1021/acsami.6b14297.

[5] B. Zhang, H. Sun, L. Wu, L. Ma, F. Xing, Q. Kong, Y. Fan, C. Zhou, X. Zhang, 3D printing of calcium phosphate bioceramic with tailored biodegradation rate for skull bone tissue reconstruction, Bio-Des. Manuf. 2 (2019) 161–171. https://doi.org/10.1007/s42242-019-00046-7.

[6] Y. Luo, A. Lode, F. Sonntag, B. Nies, M. Gelinsky, Well-ordered biphasic calcium phosphate–alginate scaffolds fabricated by multi-channel 3D plotting under mild conditions, J. Mater. Chem. B. 1 (2013) 4088–4098. https://doi.org/10.1039/C3TB20511H.

[7] M. Xu, D. Zhai, J. Chang, C. Wu, In vitro assessment of three-dimensionally plotted nagelschmidtite bioceramic scaffolds with varied macropore morphologies, Acta Biomater. 10 (2014) 463–476. https://doi.org/10.1016/j.actbio.2013.09.011.

[8] C. Wu, W. Fan, Y. Zhou, Y. Luo, M. Gelinsky, J. Chang, Y. Xiao, 3D-printing of highly uniform $CaSiO_3$ ceramic scaffolds: preparation, characterization and in vivo osteogenesis, J. Mater. Chem. 22 (2012) 12288–12295. https://doi.org/10.1039/C2JM30566F.

[9] X. Pei, L. Ma, B. Zhang, J. Sun, Y. Sun, Y. Fan, Z. Gou, C. Zhou, X. Zhang, Creating hierarchical porosity hydroxyapatite scaffolds with osteoinduction by three-dimensional printing and microwave sintering, Biofabrication. 9 (2017) 045008. https://doi.org/10.1088/1758-5090/aa90ed.

[10] A. Zocca, H. Elsayed, E. Bernardo, C.M. Gomes, M.A. Lopez-Heredia, C. Knabe, P. Colombo, J. Günster, 3D-printed silicate porous bioceramics using a non-sacrificial preceramic polymer binder, Biofabrication. 7 (2015) 025008. https://doi.org/10.1088/1758-5090/7/2/025008.

[11] K. Lin, R. Sheikh, S. Romanazzo, I. Roohani, 3D Printing of Bioceramic Scaffolds—Barriers to the Clinical Translation: From Promise to Reality, and Future Perspectives, Materials. 12 (2019) 2660. https://doi.org/10.3390/ma12172660.

[12] E. Vorndran, C. Moseke, U. Gbureck, 3D printing of ceramic implants, MRS Bull. 40 (2015) 127–136. https://doi.org/10.1557/mrs.2015.326.

[13] Q. Yu, J. Chang, C. Wu, Silicate bioceramics: from soft tissue regeneration to tumor therapy, J. Mater. Chem. B. 7 (2019) 5449–5460. https://doi.org/10.1039/C9TB01467E.

[14] K.B. Devi, B. Tripathy, P.N. Kumta, S.K. Nandi, M. Roy, In Vivo Biocompatibility of Zinc-Doped Magnesium Silicate Bio-Ceramics, ACS Biomater. Sci. Eng. 4 (2018) 2126–2133. https://doi.org/10.1021/acsbiomaterials.8b00297.

[15] C. Wu, Z. Chen, Q. Wu, D. Yi, T. Friis, X. Zheng, J. Chang, X. Jiang, Y. Xiao, Clinoenstatite coatings have high bonding strength, bioactive ion release, and osteoimmunomodulatory effects that enhance in vivo osseointegration, Biomaterials. 71 (2015) 35–47. https://doi.org/10.1016/j.biomaterials.2015.08.027.

[16] B. Leng, X. Jin, Q. Lin, L. Chen, Y. Wang, Z. Du, K. Lin, J. Chang, X. Gu, C. Wang, A comparative study of proliferation and osteogenic differentiation of rat adipose-derived stem cells in β-tricalcium phosphate (β-TCP), forsterite (Mg_2SiO_4) and clinoenstatite ($MgSiO_3$), Chin. Sci. Bull. 58 (2013) 3033–3042. https://doi.org/10.1007/s11434-013-5874-3.

[17] O.-M. Goudouri, C. Vogel, A. Grünewald, R. Detsch, E. Kontonasaki, A.R. Boccaccini, Sol–gel processing of novel bioactive Mg-containing silicate scaffolds for alveolar bone regeneration, J. Biomater. Appl. 30 (2016) 740–749. https://doi.org/10.1177/0885328215584887.

[18] H.R. Bakhsheshi-Rad, A. Najafinezhad, Z. Hadisi, N. Iqbal, M. Daroonparvar, S. Sharif, A.F. Ismail, M. Akbari, S. RamaKrishna, F. Berto, Characterization and biological properties of nanostructured clinoenstatite scaffolds for bone tissue engineering applications, Mater. Chem. Phys. 259 (2021) 123969. https://doi.org/10.1016/j.matchemphys.2020.123969.

[19] R. Choudhary, A. Chatterjee, S.K. Venkatraman, S. Koppala, J. Abraham, S. Swamiappan, Antibacterial forsterite (Mg_2SiO_4) scaffold: A promising bioceramic for load bearing applications, Bioact. Mater. 3 (2018) 218–224. https://doi.org/10.1016/j.bioactmat.2018.03.003.

[20] H. Ghomi, M. Jaberzadeh, M.H. Fathi, Novel fabrication of forsterite scaffold with improved mechanical properties, J. Alloys Compd. 509 (2011) L63–L68. https://doi.org/10.1016/j.jallcom.2010.10.106.

[21] C. Wu, Z. Chen, D. Yi, J. Chang, Y. Xiao, Multidirectional Effects of Sr-, Mg-, and Si-Containing Bioceramic Coatings with High Bonding Strength on Inflammation, Osteoclastogenesis, and Osteogenesis, ACS Appl. Mater. Interfaces. 6 (2014) 4264–4276. https://doi.org/10.1021/am4060035.

[22] S.K. Venkatraman, S. Swamiappan, Review on calcium- and magnesium-based silicates for bone tissue engineering applications, J. Biomed. Mater. Res. A. 108 (2020) 1546–1562. https://doi.org/10.1002/jbm.a.36925.

[23] X. Jin, J. Chang, W. Zhai, K. Lin, Preparation and Characterization of Clinoenstatite Bioceramics, J. Am. Ceram. Soc. 94 (2011) 66–70. https://doi.org/10.1111/j.1551-2916.2010.04032.x.

[24] S. Ni, L. Chou, J. Chang, Preparation and characterization of forsterite (Mg_2SiO_4) bioceramics, Ceram. Int. 33 (2007) 83–88. https://doi.org/10.1016/j.ceramint.2005.07.021.

[25] F. Tavangarian, R. Emadi, Mechanical activation assisted synthesis of pure nanocrystalline forsterite powder, J. Alloys Compd. 485 (2009) 648–652. https://doi.org/10.1016/j.jallcom.2009.06.051.

[26] M. Kharaziha, M.H. Fathi, Synthesis and characterization of bioactive forsterite nanopowder, Ceram. Int. 35 (2009) 2449–2454. https://doi.org/10.1016/j.ceramint.2009.02.001.

[27] F. Zhao, L. Zhang, Z. Ren, J. Gao, X. Chen, X. Liu, T. Ge, A novel and green preparation of porous forsterite ceramics with excellent thermal isolation properties, Ceram. Int. 45 (2019) 2953–2961. https://doi.org/10.1016/j.ceramint.2018.09.296.

[28] L. Chen, G. Ye, Q. Wang, B. Blanpain, A. Malfliet, M. Guo, Low temperature synthesis of forsterite from hydromagnesite and fumed silica mixture, Ceram. Int. 41 (2015) 2234–2239. https://doi.org/10.1016/j.ceramint.2014.10.025.

[29] S. Sano, N. Saito, S. Matsuda, N. Ohashi, H. Haneda, Y. Arita, M. Takemoto, Synthesis of High Density and Transparent Forsterite Ceramics Using Nano-Sized Precursors and Their Dielectric Properties, J. Am. Ceram. Soc. 89 (2006) 568–574. https://doi.org/10.1111/j.1551-2916.2005.00766.x.

[30] N. Vlasopoulos, Process for producing cement binder compositions containing magnesium, US20130213273A1, 2013. https://patents.google.com/patent/US20130213273A1/en.

[31] F. Jin, A. Al-Tabbaa, Strength and hydration products of reactive MgO–silica pastes, Cem. Concr. Compos. 52 (2014) 27–33. https://doi.org/10.1016/j.cemconcomp.2014.04.003.

[32] T. Zhang, L.J. Vandeperre, C.R. Cheeseman, Formation of magnesium silicate hydrate (M-S-H) cement pastes using sodium hexametaphosphate, Cem. Concr. Res. 65 (2014) 8–14. https://doi.org/10.1016/j.cemconres.2014.07.001.

[33] Z. Li, T. Zhang, J. Hu, Y. Tang, Y. Niu, J. Wei, Q. Yu, Characterization of reaction products and reaction process of MgO-SiO_2-H_2O system at room temperature, Constr. Build. Mater. 61 (2014) 252–259. https://doi.org/10.1016/j.conbuildmat.2014.03.004.

[34] J. Szczerba, R. Prorok, E. Śnieżek, D. Madej, K. Maślona, Influence of time and temperature on ageing and phases synthesis in the MgO-SiO_2-H_2O system, Thermochim. Acta. 567 (2013) 57–64. https://doi.org/10.1016/j.tca.2013.01.018.

[35] T. Zhang, Luc.J. Vandeperre, C.R. Cheeseman, Magnesium-silicate-hydrate cements for encapsulating problematic aluminium containing wastes, J. Sustain. Cem.-Based Mater. 1 (2012) 34–45. https://doi.org/10.1080/21650373.2012.727322.

[36] K.-Y. Hwang, J.-Y. Seo, H.Q.H. Phan, J.-Y. Ahn, I. Hwang, MgO-Based Binder for Treating Contaminated Sediments: Characteristics of Metal Stabilization and Mineral Carbonation: A Novel MgO-Based Binder for Treating Contaminated Sediments, CLEAN - Soil Air Water. 42 (2014) 355–363. https://doi.org/10.1002/clen.201200663.

[37] S.A. Walling, H. Kinoshita, S.A. Bernal, N.C. Collier, J.L. Provis, Structure and properties of binder gels formed in the system $Mg(OH)_2$-SiO_2-H_2O for immobilisation of Magnox sludge, Dalton Trans. 44 (2015) 8126–8137. https://doi.org/10.1039/C5DT00877H.

[38] F. Martini, M. Tonelli, M. Geppi, F. Ridi, S. Borsacchi, L. Calucci, Hydration of MgO/SiO_2 and Portland cement mixtures: A structural investigation of the hydrated phases by means of X-ray diffraction and solid state NMR spectroscopy, Cem. Concr. Res. (2017). https://doi.org/10.1016/j.cemconres.2017.08.029.

[39] M. Tonelli, F. Martini, L. Calucci, E. Fratini, M. Geppi, F. Ridi, S. Borsacchi, P. Baglioni, Structural characterization of magnesium silicate hydrate: towards the design of eco-sustainable cements, Dalton Trans. 45 (2016) 3294–3304. https://doi.org/10.1039/C5DT03545G.

[40] K.J.D. MacKenzie, R.H. Meinhold, Thermal reactions of chrysotile revisited: A ^{29}Si and ^{25}Mg MAS NMR study, Am. Mineral. 79 (1994) 43–50.

[41] K.J.D. MacKenzie, R.H. Meinhold, The thermal reactions of talc studied by ^{29}Si and ^{25}Mg MAS NMR, Thermochim. Acta. 244 (1994) 195–203. https://doi.org/10.1016/0040-6031(94)80219-X.

[42] A. Bigham, S.A. Hassanzadeh-Tabrizi, M. Rafienia, H. Salehi, Ordered mesoporous magnesium silicate with uniform nanochannels as a drug delivery system: The effect of calcination temperature on drug delivery rate, Ceram. Int. 42 (2016) 17185–17191. https://doi.org/10.1016/j.ceramint.2016.08.009.

[43] B. Panda, C. Sonat, E.-H. Yang, M.J. Tan, C. Unluer, Use of magnesium-silicate-hydrate (M-S-H) cement mixes in 3D printing applications, Cem. Concr. Compos. 117 (2021) 103901. https://doi.org/10.1016/j.cemconcomp.2020.103901.

[44] E.M. Van der Merwe, C. Strydom, A. Botha, Hydration of medium reactive industrial magnesium oxide with magnesium acetate, J. Therm. Anal. Calorim. 77 (2004) 49–56. https://doi.org/10.1023/B:JTAN.0000033187.61971.1d.

[45] M. Li, X. Tian, D.J. Schreyer, X. Chen, Effect of needle geometry on flow rate and cell damage in the dispensing-based biofabrication process, Biotechnol. Prog. 27 (2011) 1777–1784. https://doi.org/10.1002/btpr.679.

[46] S. Brunauer, P.H. Emmett, E. Teller, Adsorption of Gases in Multimolecular Layers, J. Am. Chem. Soc. 60 (1938) 309–319. https://doi.org/10.1021/ja01269a023.

[47] E.P. Barrett, L.G. Joyner, P.P. Halenda, The Determination of Pore Volume and Area Distributions in Porous Substances. I. Computations from Nitrogen Isotherms, J. Am. Chem. Soc. 73 (1951) 373–380. https://doi.org/10.1021/ja01145a126.

[48] D.R.M. Brew, F.P. Glasser, Synthesis and characterisation of magnesium silicate hydrate gels, Cem. Concr. Res. 35 (2005) 85–98. https://doi.org/10.1016/j.cemconres.2004.06.022.

[49] M. Tonelli, F. Martini, L. Calucci, M. Geppi, S. Borsacchi, F. Ridi, Traditional Portland cement and MgO-based cement: a promising combination?, Phys. Chem. Earth Parts ABC. 99 (2017) 158–167. https://doi.org/10.1016/j.pce.2017.01.011.

[50] M. Schmitt, P. Weiss, X. Bourges, G. Amador del Valle, G. Daculsi, Crystallization at the polymer/calcium-phosphate interface in a sterilized injectable bone substitute IBS, Biomaterials. 23 (2002) 2789–2794. https://doi.org/10.1016/S0142-9612(02)00015-7.

[51] G.R. Shetty, B.L. Rao, S. Asha, Y. Wang, Y. Sangappa, Preparation and characterization of silk fibroin/hydroxypropyl methyl cellulose (HPMC) blend films, Fibers Polym. 16 (2015) 1734–1741. https://doi.org/10.1007/s12221-015-5223-z.

[52] W.-J. Long, J.-L. Tao, C. Lin, Y. Gu, L. Mei, H.-B. Duan, F. Xing, Rheology and buildability of sustainable cement-based composites containing micro-crystalline cellulose for 3D-printing, J. Clean. Prod. 239 (2019) 118054. https://doi.org/10.1016/j.jclepro.2019.118054.

[53] M. Tonelli, F. Martini, A. Milanesi, L. Calucci, M. Geppi, S. Borsacchi, F. Ridi, Effect of phosphate additives on the hydration process of magnesium silicate cements, J. Therm. Anal. Calorim. 138 (2019) 3311–3321. https://doi.org/10.1007/s10973-019-08847-9.

[54] S.A. Walling, J.L. Provis, Magnesia-Based Cements: A Journey of 150 Years, and Cements for the Future?, Chem. Rev. 116 (2016) 4170–4204. https://doi.org/10.1021/acs.chemrev.5b00463.

[55] S.A. Kumar, Eco-Friendly Nano-Hybrid Materials for Advanced Engineering Applications, CRC Press, 2017.

[56] R. Lakshmi, Wollastonite/forsterite composite scaffolds offer better surface for hydroxyapatite formation, Bull Mater Sci. 42 (2019). https://doi.org/10.1007/s12034-019-1814-4.

[57] X. Li, Q. Huang, T.A. Elkhooly, Y. Liu, H. Wu, Q. Feng, L. Liu, Y. Fang, W. Zhu, T. Hu, Effects of titanium surface roughness on the mediation of osteogenesis via modulating the immune response of macrophages, Biomed. Mater. 13 (2018) 045013. https://doi.org/10.1088/1748-605X/aabe33.

[58] Q. Huang, T.A. Elkhooly, X. Liu, R. Zhang, X. Yang, Z. Shen, Q. Feng, Effects of hierarchical micro/nano-topographies on the morphology, proliferation and differentiation of osteoblast-like cells, Colloids Surf. B Biointerfaces. 145 (2016) 37–45. https://doi.org/10.1016/j.colsurfb.2016.04.031.

[59] D.D. Deligianni, N. Katsala, S. Ladas, D. Sotiropoulou, J. Amedee, Y.F. Missirlis, Effect of surface roughness of the titanium alloy Ti–6Al–4V on human bone marrow cell response and on protein adsorption, Biomaterials. 22 (2001) 1241–1251. https://doi.org/10.1016/S0142-9612(00)00274-X.

[60] C.H. Giles, D. Smith, A. Huitson, A General Treatment and Classification of the Solute Adsorption Isotherms-Part I. Theoretical, J. Colloid Interface Sci. 47 (1974) 755–765. https://doi.org/10.1016/0021-9797(74)90252-5.

[61] C.H. Giles, A.P. D'Silva, I.A. Easton, A General Treatment and Classification of the Solute Adsorption Isotherms-Part II. Experimental Interpretation, J. Colloid Interface Sci. 47 (1974) 766–778. https://doi.org/10.1016/0021-9797(74)90253-7.

[62] K. S. W. Sing, D. H. Everett, R. A. W. Haul, L. Moscou, R. A. Pierotti, J. Rouquerol, T. Siemieniewska, Reporting physisorption data for gas/solid systems, Pure Appl Chem. 57 (1985) 603–619. https://doi.org/10.1351/pac198557040603.

[63] A.H. Touny, P. Sikder, M.M. Saleh, S.B. Bhaduri, Facile synthesis and characterization of biphasic magnesium phosphate bioceramic nanosheets by a reflux approach, Mater. Res. Express. 6 (2019) 095007. https://doi.org/10.1088/2053-1591/ab2bb5.

[64] F. Martini, S. Borsacchi, M. Geppi, M. Tonelli, F. Ridi, L. Calucci, Monitoring the hydration of MgO-based cement and its mixtures with Portland cement by ^{1}H NMR relaxometry, Microporous Mesoporous Mater. (2017). https://doi.org/10.1016/j.micromeso.2017.05.031.

[65] L.-C. Gerhardt, A.R. Boccaccini, Bioactive Glass and Glass-Ceramic Scaffolds for Bone Tissue Engineering, Materials. 3 (2010) 3867–3910. https://doi.org/10.3390/ma3073867.

[66] A. Khalil, X. Wang, K. Celik, 3D printable magnesium oxide concrete: towards sustainable modern architecture, Addit. Manuf. 33 (2020) 101145. https://doi.org/10.1016/j.addma.2020.101145.

[67] M. Bonini, Physico-Chemical Challenges in 3D Printing of Polymeric Nanocomposites and Hydrogels for Biomedical Applications, J Nanosci Nanotechnol. 21 (2021) 2778–2792. https://doi.org/10.1166/jnn.2021.19063.

7:Supplementary Material

Video

Credit author statement

Monica Tonelli: Conceptualization, Methodology, Formal analysis, Investigation, Writing - Original Draft, Writing - Review & Editing, Visualization
Andrea Faralli: Conceptualization, Methodology, Formal analysis, Investigation
Francesca Ridi: Conceptualization, Methodology, Formal analysis, Writing - Original Draft, Writing - Review & Editing, Visualization, Project administration, Funding acquisition
Massimo Bonini: Conceptualization, Methodology, Formal analysis, Investigation, Writing - Original Draft, Writing - Review & Editing, Visualization, Supervision, Project administration, Funding acquisition